https://ntrs.nasa.gov/search.jsp?R=20180005433 2019-04-29T07:47:11+00:00Z

Optical Characterization of Fuel Injection in a Flame Tube Combustor Using a GE TAPS Injector Configuration

Yolanda R. Hicks,[1] Tyler G. Capil,[2] Robert C. Anderson,[3]
NASA Glenn Research Center, Cleveland, Ohio, 44135, USA

This paper presents results in which we compare fuel staging and its effect on fuel spray pattern, velocity and speciation during combustion for several inlet conditions using a GE TAPS injector configuration. Planar laser-induced fluorescence (PLIF), particle image velocimetry (PIV) and phase Doppler interferometry (PDI) were used to investigate spray patterns and velocity. The 2D PIV provides slices in the flow of axial-vertical or axial horizontal velocity components. With 3D PDI, we obtained 3 components of velocity, and fuel drop sizes. Chemiluminescence imaging and spontaneous Raman scattering (SRS) were used to investigate flame structure, species location and relative species concentration. Phase Doppler and PIV data were acquired using scatter from fuel droplets; therefore, those data were obtained only at the pilot-only test points. Raman measurements were acquired only at 10/90 split points to avoid droplets.

Nomenclature

AST	=	Advanced Subsonic Technology
CRZ	=	central recirculation zone
EINOX	=	emission index for oxides of nitrogen
ERA	=	Environmentally Responsible Aviation
FAR	=	fuel-to-air ratio
FWHM	=	full width at half maximum
GRC	=	Glenn Research Center
LTO	=	landing-takeoff cycle
NOx	=	nitrogen oxides, oxides of nitrogen
P3	=	combustor inlet pressure
PDI	=	phase Doppler interferometry
PIV	=	particle image velocimt
PLIF	=	planar laser-induced fluorescence
PLS	=	planar laser scatter
RMS	=	Root-Mean-Square
SLTO	=	sea level takeoff
SRS	=	spontaneous Raman scattering
T3	=	combustor inlet temperature
UV	=	ultraviolet

I. Introduction

EMISSIONS of oxides of nitrogen (NOx) have long been a concern in the aviation industry because NOx contributes to smon at lower altitudes and may negatively aafect the protective ozone layer at high altitude. Lowering fuel burn is achieved through gains in thermodynamic efficiency and also has benefits, both economic and environmental. Efficiency gains may be achieved by increasing the engine operating pressure ratio, which increases combustor inlet temperature; however, NOx formation rates increase with higher temperatures. Without an improvement in combustor technology, higher efficiency engines will have higher, not lower, NOx emissions: improved low-NOx combustor technologies need to be developed.

---

[1] Research Engineer, Combustion Branch
[2] Research Engineer, Optics and Photonics Branch
[3] Senior Engineer, Optics and Photonics Branch

General Electric Aviation (GE) explored the Twin Annular Premixing Swirler (TAPS) injector concept[4,5] in the mid-1990s, and proposed TAPS as its primary approach to achieve NASA's Advanced Subsonics Technology (AST) initiative to reduce NOx emissions below 60% of the 1996 ICAO standards, while maintaining low CO emissions. Over the years, NASA has tested selected TAPS research hardware in GRC combustor facilities, during contractual collaborations under AST, the Ultra Efficient Engine Technology (UEET), and Fundamental Aeronautics Programs. Figure 1 illustrates the TAPS injection concept.

In this paper, we revisit flame tube testing of one research TAPS injector. Specifically, the primary objective for this study was to compare fuel staging and its effects on fuel spray pattern, velocity and fuel droplet sizes, and speciation during combustion. The comparison was enabled through the use of several optical and laser-based measurement techniques. Planar laser induced fluorescence of OH was used to emphasize fuel spray patterns as well as locations of the primary reaction zone. Chemiluminescence imaging enabled qualitative visualization of key excited, nascent species of combustion including CH*, C2*, OH*, and NO*. 2D particle image velocimetry measured axial and cross-flow velocities which were used to characterize the TAPS injector's flow field performance in regards to fuel spray. Additional measurements from phase Doppler interferometry also provided 3-component velocity measurements as well as fuel droplet sizes. Spontaneous Raman spectroscopy was implemented in these tests to examine speciation and temperature.

In the following, we briefly describe the TAPS Hardware, the experimental setup and test matrix. This is followed by a description of the optical diagnostics used. The results and discussion section presents PLIF results, velocity and droplet size results, chemiluminescence imaging results, and results from spontaneious Raman scattering diagnostics.

II. TAPS Hardware

The TAPS injector concept, illustrated in Fig. 1 and described in Refs. 4-6, consists of a pilot stage and a main stage, with turndown controlled by shifting the fuel distribution between the stages. As seen in this TAPS concept sketch, the pilot fuel circuit injects a conical spray from the center of the cup. When running in pilot-only mode, this zone is locally fuel-rich for added stability. The main fuel circuit feeds a number of discrete jets-in-crossflow into the surrounding annular passage as a means to promote fuel breakup, vaporization and some premixing with the incoming air before exiting the dome. Swirl is imparted to the air that flows through each circuit.

III. Experiment Setup

A. TAPS Installation

The combustor subcomponent facility at NASA Glenn supplies heated, non-vitiated air to the test rig. The test rig uses a castable ceramic to form the combustor "liner". A single TAPS cup was installed in the rig using a cylindrical cast liner, with cutouts for optical access. The TAPS injector was installed such that the optics could probe the region immediately downstream of the dump plane in the mixing region between the pilot and main circuits.

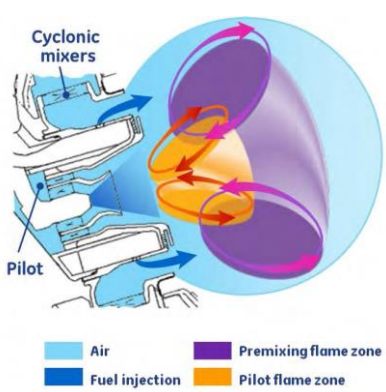

Figure 1. TAPS injection concept[6]

Test Matrix

The primary inlet conditions used are shown in Table 1. The specific inlet conditions are not from any particular engine size class or cycle, but we normalized the fuel/air ratio based on a large engine Generation-2 ERA cycle. Temperatures and pressures are de-rated from higher power conditions due to facility limitations. Four fuel splits were run between pilot and main: 100%, 60%, 20%, and 10% pilot. For

selected points, we also ran high-low cases for fuel/air ratio.

.

Table 1. Primary conditions used for TAPS fuel injection tests.

Test Point	P_3 psia	T_3 °F	Fuel Split % Pilot/Main	FAR/FAR_{SLTO}
1	166	650	100/0	0.54
2	135	720	100/0	0.70
3	200	925	60/40	0.71
4	250	1000	20/80	0.84
5	250	1000	10/90	0.74
6	150	1000	10/90	0.74

B. Optical Diagnostics Setup and Procedures

Five techniques were used to examine the TAPS injector flow field immediately downstream of the dome dump plane, in a region between the pilot and main circuits. Planar laser-induced fluorescence (PLIF) of fuel and OH was used to determine fuel spray patternation and image the reaction zone. Chemiluminescence imaging of radical combustion species C2*, CH*, OH*, and NO* (with emissions at 515-nm, 427-nm, 306-nm, 237-nm) was also used for reaction zone flame structure. 2D planar image velocimetry (PIV) ws used to determine the axial and cross-flow velocities, particularly of the fuel spray. Phase Doppler interferometry (PDI) was used to measure fuel droplet velocities and sizes. Spontaneous Raman scattering (SRS) was used to measure combustion species and temperature.

PLIF and chemiluminescence images were acquired for all conditions shown in the test matrix. Because we relied on droplets for the velocity measurements, PIV and PDI data were acquired only at the pilot only (100/0) split conditions, which also had the lowest T_3 and P_3. For SRS, we wanted to avoid droplets, so obtained data only at 10/90 split conditions.

All speciation images (PLIF and chemiluminescence) we obtained using intensified CCD (ICCD) camera having a Gen II Super Blue, Slow gate intensifier. The gate time used was 50-ns. For PLIF, the laser was a 10-Hz, frequency-doubled Nd:YAG-pumped dye laser/frequency mixer system set to produce wavelengths around 282-nm. A laser was not used for chemiluminescence images.

Chemiluminescence imaging has become increasingly popular as a simple way to visualize the reaction zone via OH*, CH*, and C2* [refs c1- c4]. Several authors have used chemiluminescence to determine reaction rates, determine zone thicknesses, primarily in premixed methane/air flames[refs]. There have also been studies to quantify imaging of these species, which involves measuring and accounting for the broad signal from CO2* that overlaps these species [Guyot et al]. Guiberti et al[ref] determined that while CO2* interference with CH* was significant, interference to OH* was not. The chemiluminescence images presented here are not corrected for any spectral interferences.

When obtaining OH PLIF, we typically get relatively strong background interference near the dome because refined JP-class fuels have up to 25 percent aromatics by volume; certain of these aromatics, such as methyl-benzenes and naphthalenes, are broadband absorbers and emitters in the same wavelength region we use to excite OH [refs]. Therefore, to obtain OH PLIF, we collected raw fluorescence signal when tuned to the $R_1$1 line in the (1,0) band and collected light from the (1, 1) band using a filter centerd near 313-nm. We then tuned off the excitation line to collect background light from the fuel. We designated this fuel fluorescence Fuel-313. Fuel-313 is subtracted from the raw OH PLIF signal to render OH PLIF images. Because the peak fuel fluorescence is near 330-nm, we also obtained fuel PLIF using a filter centered at 334-nm and designate that fuel PLIF as fuel-334. The two sets of fuel PLIF were obtained at the same time using cameras on opposite sides of the combustor.

The Raman setup was used to explore the Stokes/Anti-Stokes method for deriving combustion temperature. As such, the spectrometer grating was chosen to obtain both nitrogen peaks, at 2331cm^{-1} from the laser line. Although we think this method has potential, the small inlet temperature range available limited our ability to calibrate the system. Speciation was still possible, even though the spectral range restricted the region of species available to that between CO_2 and N_2.

Specific Setup Details

Using a setup similar to that shown in Figure 2a (one camera on either side, with light collected from an angle perpendicular to the combustor flow direction) we acquired two-dimensional images of OH and fuel PLIF, and chemiluminescence images of C2*, CH*, OH*, and NO*.

The OH, fuel-313 PLIF, CH*, OH*, and NO* images were obtained using the same receiving optics and intensified ICCD camera. The second ICCD camera was used to record fuel-334 PLIF and C2*. Remotely controlled filter wheels allowed us to select a species-specific filter (FWHM of 10-nm, typical) to pass light through a UV-grade, f = 105-mm, f/4.5, macro camera lens. The light was then focused onto a gated, 16-bit, 1k × 1k pixel array, ICCD camera (Princeton Instruments PIMAX) having a Gen II Super-Blue-Slow-Gate intensifier. The laser beam was formed into a sheet using a pair of cylindrical lenses, to obtain a sheet approximately 300-µm thick. We typically acquired images with on-chip averages of 200 gates, and traversed across the flow along the Y axis in 1-mm increments. The laser sheet and collection optics were traversed together so as to maintain focus on the laser sheet. For chemiluminescence, we did not use the laser and collected light with the camera focused on a plane at Y=0 (coincident with the injector centerline) using species-specific filters centered at 514-nm, 432-nm, 313-nm, and 237-nm for C2*, CH*, OH*, and NO*, respectively.

The 2D PIV images were also acquired using a setup similar to Fig. 2a. The laser used was a dual head, frequency-doubled Nd:YAG laser operating at 15-Hz. The camera was a frame transfer CCD with 1200 x 1600 pixel resolution. As with PLIF, the laser sheet and camera was traversed across the flow, in 1-mm increments. We also used an alternate setup, with the camera positioned above the combustor and inserted a horizontal laser sheet through the side window. We collected 300 image pairs to produce instaneous vector fields as well as an average 2D vector field.

Phase Doppler data were acquired using a setup similar to the schematic shown in Fig. 2b, which shows the transmitter and receiver angle downward in order to access the area more directly downstream from the TAPS pilot region. The transmitter-receiver were set up in 30° forward scatter arrangement, each at 15° with respect to the horizontal. Three non-orthogonal components were obtained using a three-color system via a single transmitter, so two geometric transforms were applied to the collected raw signal—one for the optical system, the other because of the 15° tilt—so that the velocity vectors conformed to the

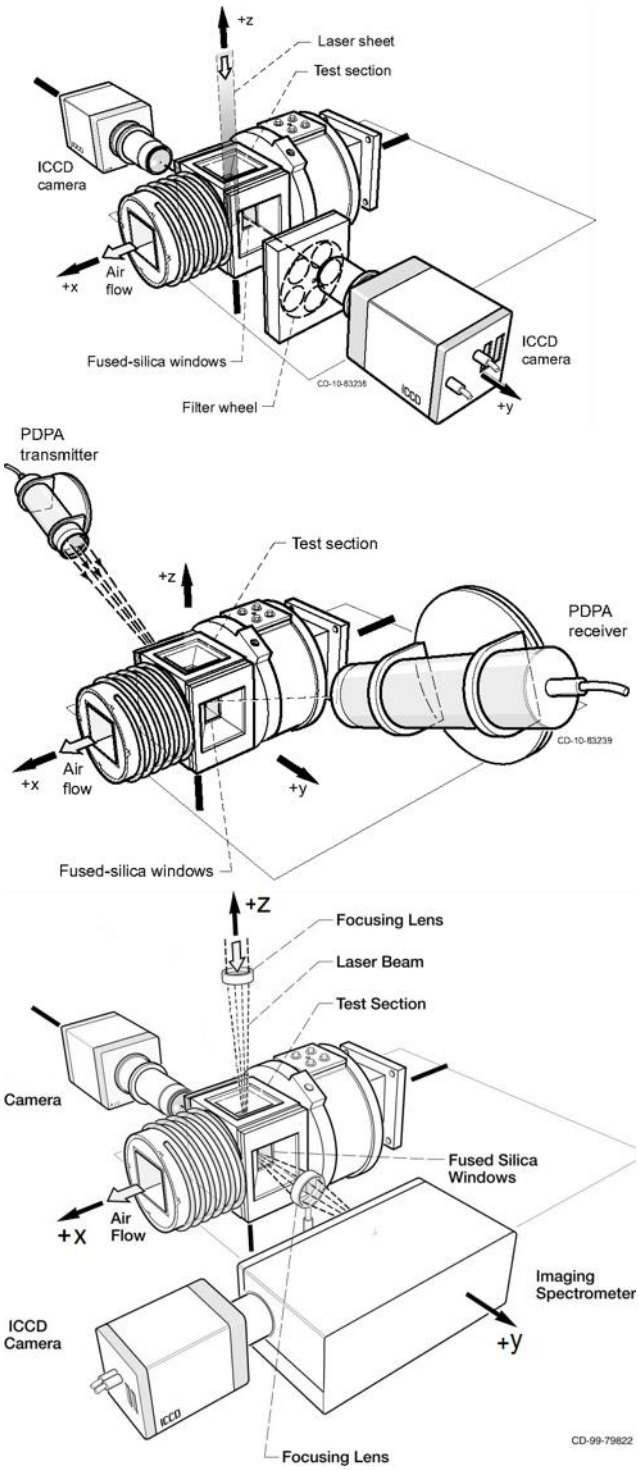

Figure 2. Schematic drawings that shows typical components and configuration used for top) 2D imaging methods: (a) planar laser-induced fluorescence, PIV, and chemiluminescence; (b) center: Phase Doppler Interferometry; (c) bottom: Raman spectroscopy.

convention we used for the combustion system. The available optic access limited the traverse range in the axial direction to approximately 6-mm.

Raman spectra were acquired using a setup shown in the schematic from Figure 2c. A 30-Hz frequency doubled Nd:YAG laser beam was focused on a point in the flow path. The Raman signal was captured by a 60-mm, f/2.8, micro-Nikkor lens coupled to a fiber optic. The fiber optic was then coupled to the spectrometer and imaged onto an Andor iStar 734, intensified CCD camera. The spectrometer used a 300-groove/mm grating blazed at 500-nm. The fiber optic consisted of 37 fibers which were aligned vertically along the z-coordinate. Furthermore, the 37 fibers were binned together to form 10 strips. For the results presented here, spectra were collected with 2000 laser shots for on-chip averages. Raman scattering was collected along the x-coordinate, typically traversing from -15 mm to 15 mm in 5 mm increments. Overall, this provides a total spatial view on the order of 30 mm in the x-direction, and about 4 mm in the z-direction. The Raman data presented in this paper was limited to the 10/90 split conditions.

IV. Results and Discussion

In this section, we present results from chemiluminescence and the laser-based techniques, PLIF, SRS, PIV and PDI. For these results, images are plotted either as side views, with flow from left to right; or as end views, from an aft looking forward perspective. In either case, the vertical axis plots the relative distance from the TAPS centerline. Keep in mind the field-of-view is the region immediately downstream of the dome. The probe volume visible through the windows allows us to observe the intersection of the pilot and pre-mixing flame zones.

PLIF results

Figure 3 shows results obtained for a pilot-only case (fuel split 100/0), test point 1. As we describe the results for this inlet condition, we also use this point to discuss some pros and cons for this implementation of the PLIF measurement and the combusting system. Figures 3a and 3b show color contours of OH PLIF. Figure 3a is a side view at Y = 0 with flow from left to right. Figure 3b shows an end view composite slice at one axial position, with flow out of the page. The image in figure 3c is the composite background signal when the laser is tuned away from the OH excitation line, captured using the same optical filtering as when the laser is tuned to the excitation line; the OH images presented represent this off-line signal subtracted from the on-line signal. The image in figure 3d was acquired using a different camera on the opposite side of the combustor. This image was acquired at the same time as the background fuel PLIF, but using a filter centered at 334-nm, which is closer to the peak of fuel fluorescence and spectrally not near OH fluorescence.

With respect to the end views, the camera used to acquire the OH and background fuel PLIF images was on the right (Figure 3d) and the fuel only camera was on the left (Figure 3c). The combusting system is optically thick so that the fluorescence signal is considerably weaker on the side away from the camera. Evidence of this thickness is most apparent in the pilot-only cases, which have a higher local number density than the conditions with fuel splits. Given that we were looking at relative trends, we did not attempt to correct for multiple scattering and absorption of the laser.

When we compared the two optical filtering techniques for fuel PLIF, we determined that the two methods gave us identical information, but we had stronger signal using the 334-nm filter, so all following fuel PLIF images used the 334-nm filter.

The fuel PLIF images show an annular ring of fuel that is relatively uniform in distribution within the annulus and symmetric about the center position. The OH PLIF images show two zones of OH: a region of high signal emanating from the pilot spray, and a region where OH forms on the fuel-lean side of the spray in the shear layer mixing region. In previous work when comparing the locations of fuel and OH, we generally saw a shift in OH to the air side of the fuel spray [ref GE2016, 9pt], but the shift in the OH signal with respect to fuel near the dome in this case is very slight or not present. The contour lines in figure 3a show the fuel position relative to the color contour of OH PLIF. This may indicate very little mixing at this condition.

Figure 4 shows fuel PLIF (top row) and OH PLIF for the 60/40 fuel split condition. The left column shows the side view and the second and third columns show end views at two axial locations. The fuel PLIF shows a uniformly-distributed pilot region but very distinct regions of stronger fuel signal from the main injector. The OH side view image indicates a bimodal axial distribution and shows most of the signal on the outside of the fuel PLIF location. We saw a similar pattern in the OH* chemiluminescence signal for this condition (see Fig. 7). Also there is evidence of optical thickness, since the right-hand side of the end views shows a fairly uniform OH distribution in the region between the pilot and main fuel circuits while the left-hand side does not

Figures 5 and 6 present end view composites of fuel and OH at P3 of 250-psia, with axial position increasing from left to right in each row. Each column is nominally at the same axial position, beginning at the dome. Because good

fuel signal does not extend as far downstream as the OH signal because the fuel is consumed in the combustion process, we limit the fuel PLIF images to within the first xx-mm from the dump plane.

In both Figs. 5 and 6, the top row is from 20/80 fuel split condition. The next two rows show the 10/90 split conditions with equivalence ratios 10% below and above that for the 20/80 split condition. Fuel patternation is similar in all three cases. Fuel (Fig. 5) from the pilot region is barely perceptible and, although there is still separation between the individual main circuit injection sites, the overall fuel distribution is more uniform than we observed for the 60/40 fuel split condition shown in Fig. 4. Other differences are observed when looking at OH distribution (Fig.6) compared to the 60/40 split, particularly farther downstream. The 20/80 split shows a more uniform distribution, whereas for the 10/90 split, relatively little OH is produced within the inner part of the cone, in the lower part of the images..

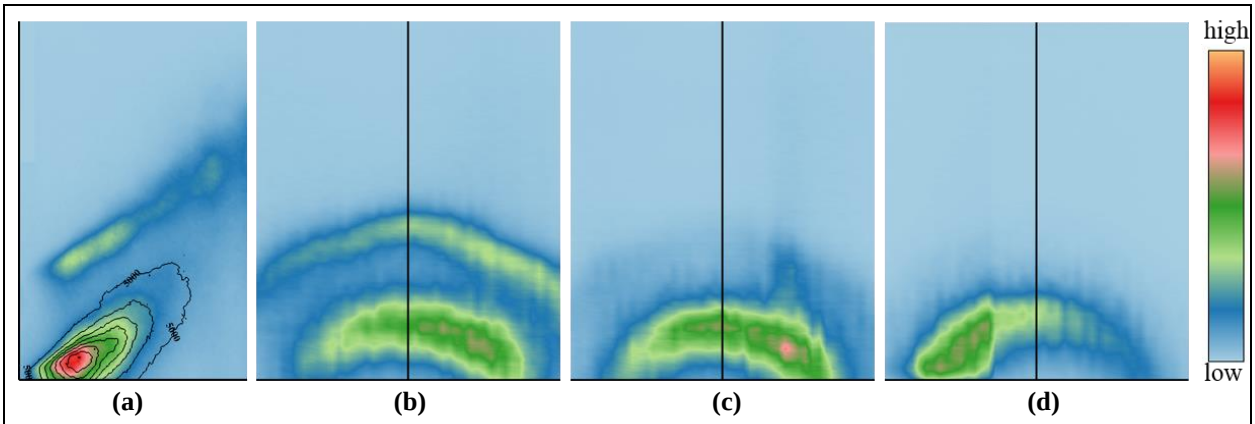

Fig. 3 PLIF Results obtained for a pilot-only case (fuel split 100/0), test point 1. a) OH PLIF side view at Y=0, b) OH PLIF composite end view slice, c) composite end view background with laser tuned away from OH, d) OH PLIF with filter centered at 334nm. Line contours in a) denote location of fuel PLIF signal for comparison with OH PLIF.

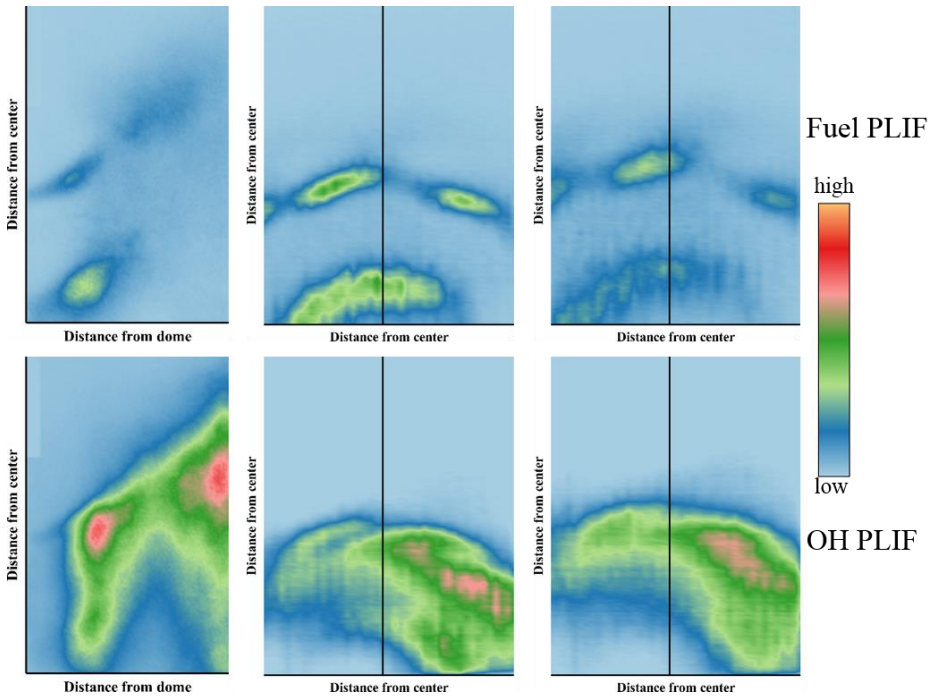

Figure 4 PLIF Results obtained for a the 60/40 fuel split, test point 3. Top row: fuel-334, bottom row: OH. The first column shows the side view at Y=0, the second and third columns show composite end views at two axial locations.

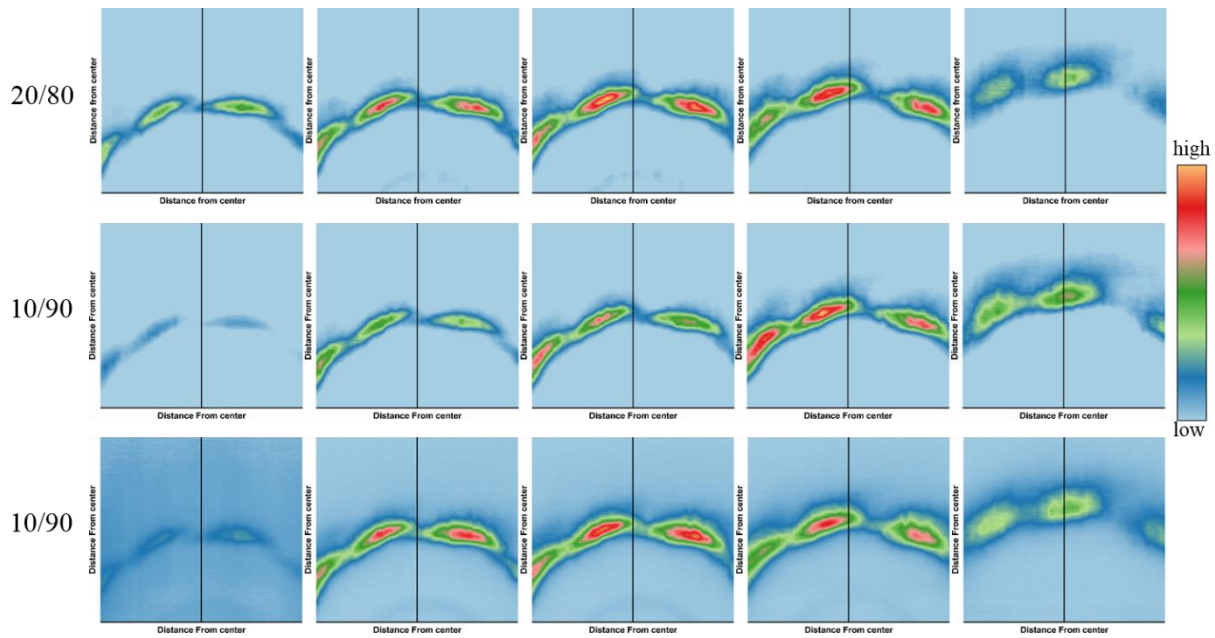

Figure 5 Fuel pattern as revealed by fuel PLIF composites at five axial locations (columns) for three inlet conditions (rows). The distance from the dump plane increases from left to right.

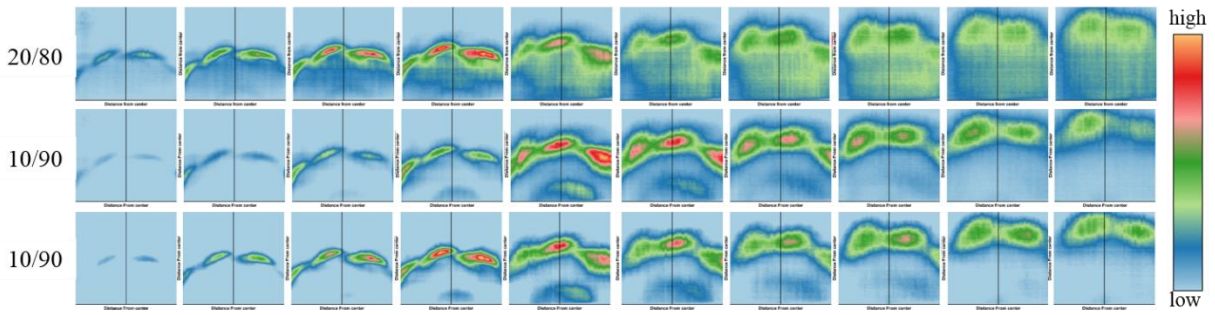

Figure 6. End view composites of OH via PLIF. Each column shows an axial slice. Distance from dump plane increases from left to right. The first five columns correspond to the axial locations for fuel PLIF in Fig. 5.

Figure 7 shows chemiluminescence images from eight variations of inlet condition (rows), for species (columns, left to right) CH*, C_2*, OH*, and NO*. Flow is left to right. Because the variation in signal was so great, each C2* and CH* image is individually scaled. OH* and NO* are scaled per specie. Each image is a line-of-sight average through the flow field rather than spatially-resolved as with PLIF.

We note first that NO* tends to track well with OH* regardless of fuel split. This is reasonable because bulk [OH*] follows flame temperature [ref]. Second, differences between CH* and C2* are best revealed when comparing the 20/80 and 10/90 fuel splits. Although for the 20/80 split, the signal from the main region is lower than the pilot for both species, C_2* main chemiluminescence is nearly absent, whereas for 10/90, pilot and main C2* signals are of the same order, but CH* signal is higher in the main than from the pilot region Also, for these conditions, CH* tracks more with OH*; this volume is likely to indicate the main fuel/air mixing and burning zone.

We also note that the heavily-fueled pilot splits of 100/0 and 60/40 have much different flame structure compared to the 20/80 and 10/90 fuel split conditions, particularly between the predominantly fuel side species (CH*, C2*) and the air side (OH*). For the cases that have higher pilot fuel flow, the reactions persist through the full axial extent of the field of view, and is consistent with a locally fuel-rich system. We also saw quite high luminosity from C2* and CH*, indicating lots of fuel breakdown occurring and possible soot formation. (The signal at these conditions far exceeded that from the 20/80 and 10/90 fuel split conditions, by roughly two orders of magnitude, which is why each

image showing C2 and CH is self-scaled.) Near the dump plan is a region of moderately high C2* and CH*, but most of the heat release due to those species is downstream, near the end of the field-of-view. In the gap between those maxima is where OH*forms, as well as along the air side of the reactant conical plume. NO* forms predominantly within that plume.

Aside from the differences noted previously between C2* and CH*, the 20/80 and 10/90 split cases reveal similar structure for all species, particularly near the mains.

Finally, we note the similarities between OH*chemiluminescence and OH PLIF signals for the 100/0 and 60/40 split conditions (rows 1 and 3 of figure 7; side views of figures 3 and 4). Because the source of fuel PLIF comes from aromatics, primarily naphthalenes and methyl-benzenes.

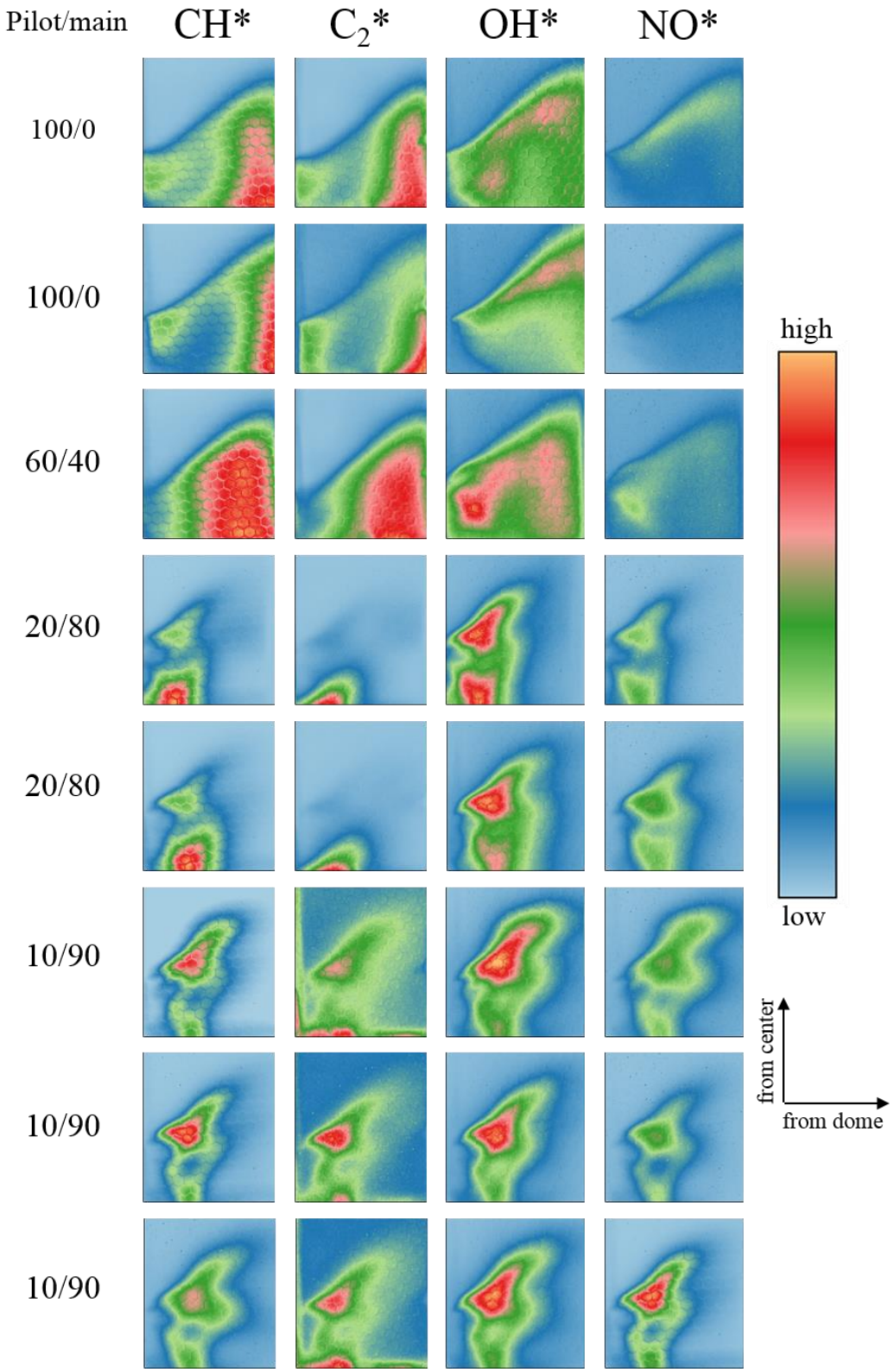

Figure 7. Chemiluminescence images from eight variations of inlet condition (rows), for species (columns, left to right) CH*, C_2*, OH*, and NO*. Flow is left to right. Images from CH* and C2* are independently-scaled. Images for OH* and NO* are scaled for each species group.

Velocity and Droplet Size Results—Pilot only inlet conditions We wanted to determine the central recirculation zone (CRZ) size and the magnitude of reverse axial velocity. Given the optical access, we could not access the region near the centerline using our 2D PIV system. We therefore used the phase Doppler interferometer to explore the area near the TAPS centerline to obtain 3 velocity components and to measure droplet sizes. Our setup did not allow access to the dump plane region, where we might expect to see strong reverse flow. The results from the PDI, shown in figures 8 and 9, indicate that our measurement locations were likely just downstream of the CRZ because the magnitude of reverse flow was very small compared to the downstream velocity. Figure 8 shows the velocity field for the pilot only condition, point 1, at two axial positions. The left image shows a contour of the axial velocity field, which features a central zone of lower velocity. As one moves outward from the center, the axial velocity increases, which is consistent with the zone of the conical fuel spray. The left image has an overlay of the horizontal-vertical (y-z) vectors and shows the core flow moves in a counterclockwise direction which agrees with the swirl imparted. Figure 9 provides some droplet statistics over the traverse range available for four axial positions. The plots include data from the most upstream to the farthest downstream locations that had enough droplets counted for good statistics. The histograms on the top row show that most droplets have a mean diameter of about 30 microns. The scatter plots indicate axial velocity as a function of linear droplet size, D_{10}. Only a relative few droplets travel upstream, which is another indicator that the region probed is at the downstream edge of the CRZ.

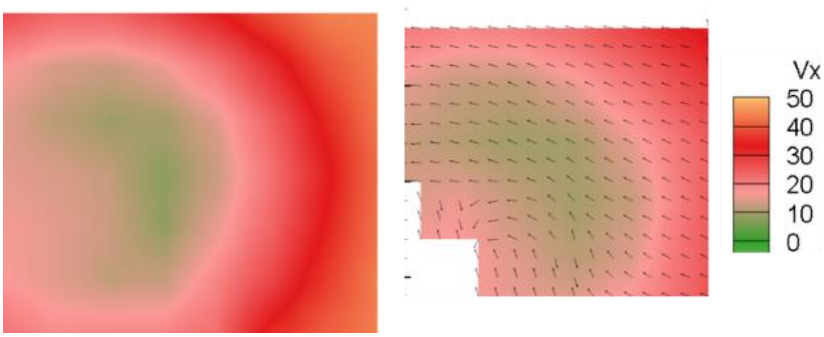

Figure 8 PDI result, test point 1. Contours of average velocity field at two axial locations. Plot on right includes vectors representing the horizontal-vertical velocity components.

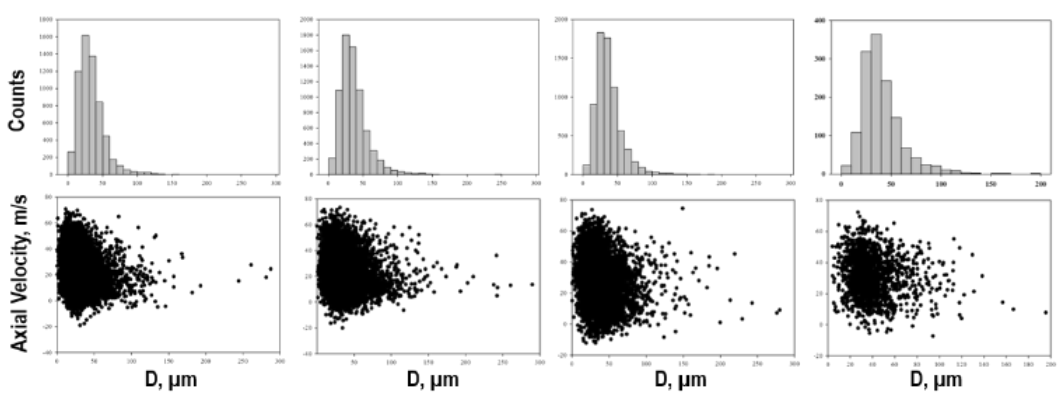

Figure 9 PDI result, test point 1. Distribution of droplet size, D10, at four axial locations. Top row shows droplet size histograms. Bottom row shows distribution of droplet size with axial velocity.

The 2D velocity data were acquired using PIV. We used two setups. In the first, a pair of laser sheets was sent vertically through the top window, to obtain axial-vertical (X-Z) velocity components. In the second configuration,

we used horizontal laser sheets and positioned the camera above the rig, to obtain axial-horizontal (X-Y) components. Figure 10 shows the axial-vertical velocity field for point 2 (pilot only) at a Y-position that corresponds to the position of the main, as shown in the inset figure of fuel PLIF. The key feature to highlight is the recirculation region near the dome and in the shear region between the pilot and main regions.

Figures 11 and 12 are from test point 1. They show axial-horizontal velocity components at the closest position to the centerline we could given the field of view, which is roughly a slice near the outer radius of the pilot region. Figure 12 features the fuel spray cone and reflects the counterclockwise swirl direction observed using PDI. Figure 11 shows a result using seeded air, in which can be seen near the bottom, a region of high downstream velocity. This is probably due to the nitrogen purge through the main fuel circuit, used to help prevent fuel line coking.

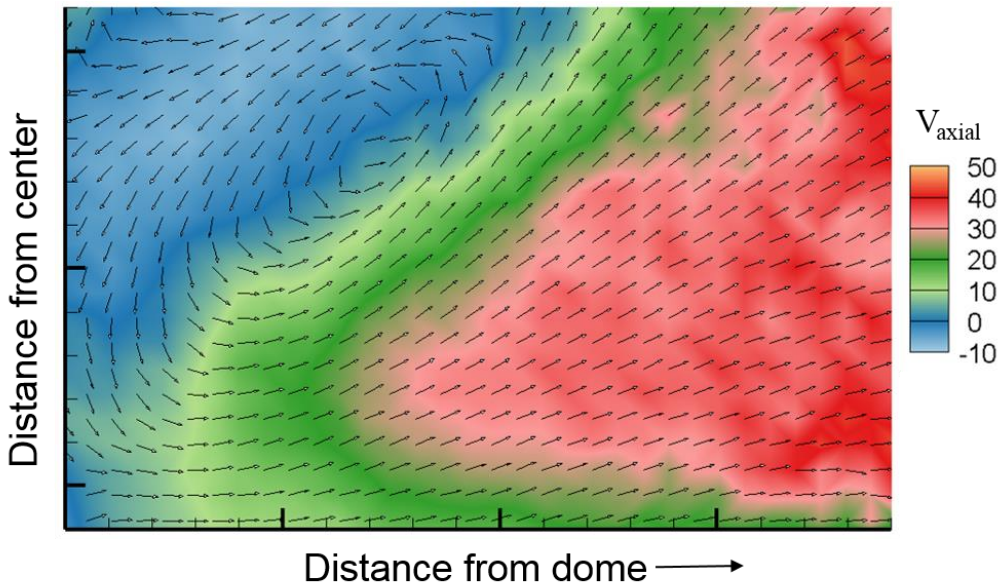

Fig. 10 PIV result. Average axial-vertical velocity field of the air, in the Y-plane near the edge of a main injection site, test point 2. Color contour is of axial velocity.

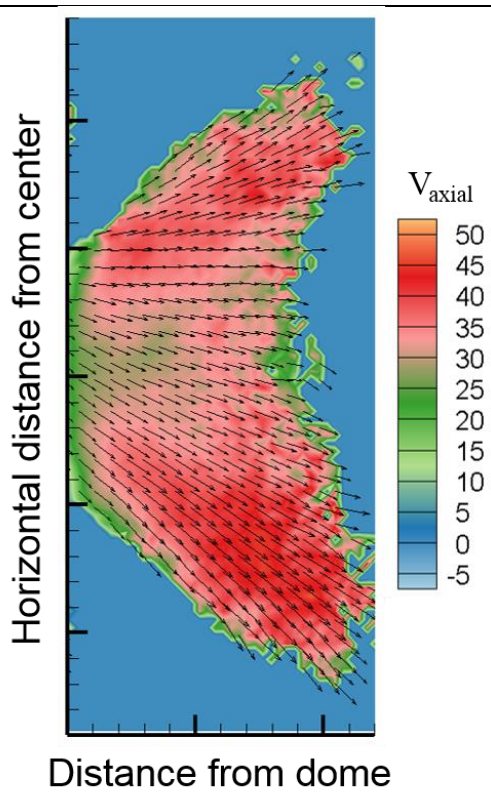

Fig 11 PIV result. PIV result. Average axial-horizontal velocity field of the fuel spray, in the region near the upper arc of the pilot for test point 1. Color contour is of axial velocity.

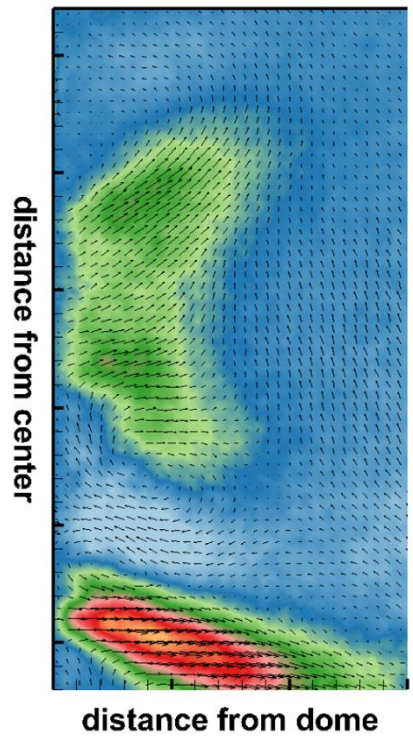

Fig 12 PIV result. Average axial-horizontal velocity field of the air, in the region near the upper arc of the pilot for test point 1. Color contour is of axial velocity.

Spontaneous Raman Scattering Results—10/90 Split inlet conditions

An example of Raman spectra acquired during these tests is shown in **Error! Reference source not found.**13 for test point xx at x = 0. The spectra were processed to remove t and smoothed using a Lee filter. Only rows 3-9 were used here due to blurring of the spectra in rows 1 and 2 due to minor issues with light hitting the collection optics. Raman peaks for nitrogen, oxygen, NO and CO_2 are available for analysis.

Of interest in this paper is a qualitative measurement of NO. The Raman spectra may be used to shed light on the amount of NO at points throughout the probed flow path. Specifically the area under the NO peak, or total signal from NO, was calculated to estimate the amount of NO for a few test conditions. The NO peak area was normalized by the area under the Stokes N_2 line to account for minor differences in collection efficiency between test points. It should also be noted

that the Raman measurements were not calibrated to provide exact quantitative measurements of species concentrations.

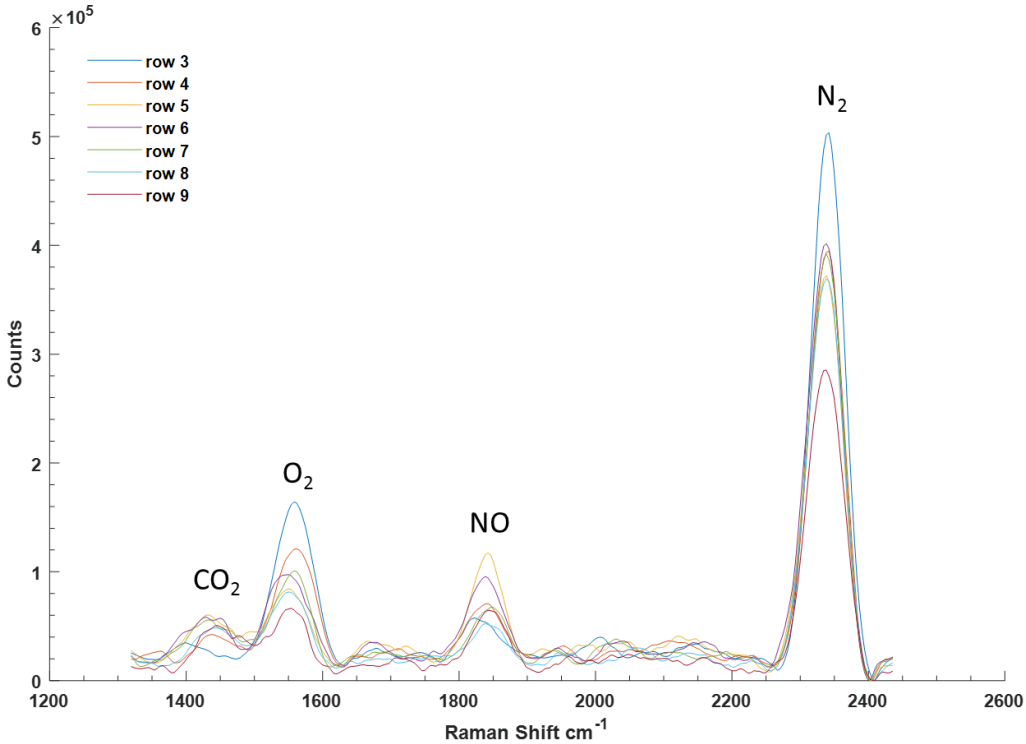

Figure 13. Sample spectra from test point xx at x = 0. Multiple spectra corresponding to each binned row of the fiber optic are shown.

Figure 14 shows a center plane slice of the OH PLIF with an overlaid box showing where the Raman data was measured. OH PLIF shows the primary flame zone where the hottest flame temperatures are expected. In Figure 14 there are two distinct regions: the bottom bulk of the OH PLIF signal originates from the pilot and the larger signal spreading through the upper portion of the image is from the main. Although much of the Raman signal acquired during these tests didnot explicitly probe the pilot or main flame, the probe area does give a sense of pilot and main interaction.

Qualitative species maps for NO at four 10/90 split conditions is shown in Figure 15 where the abscissa shows the axial distance from the dome and the ordinate shows the vertical distance above the centerline. The counts were the ratio of the NO and N_2 areas multiplied by the differential Raman scattering cross section.

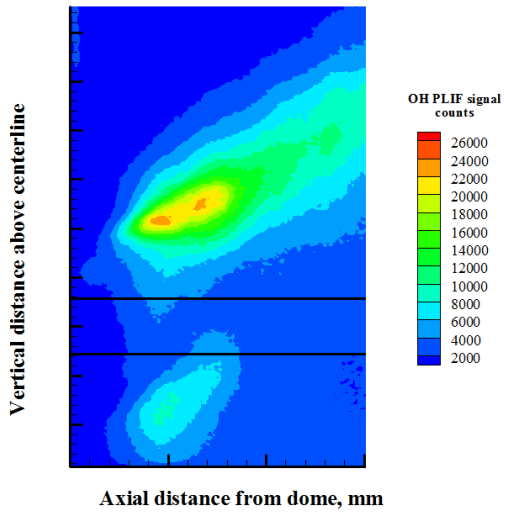

Figure 14**. OH PLIF for a particular 10/90 split condition, which highlights an overlaid box where the Raman data was probed.**

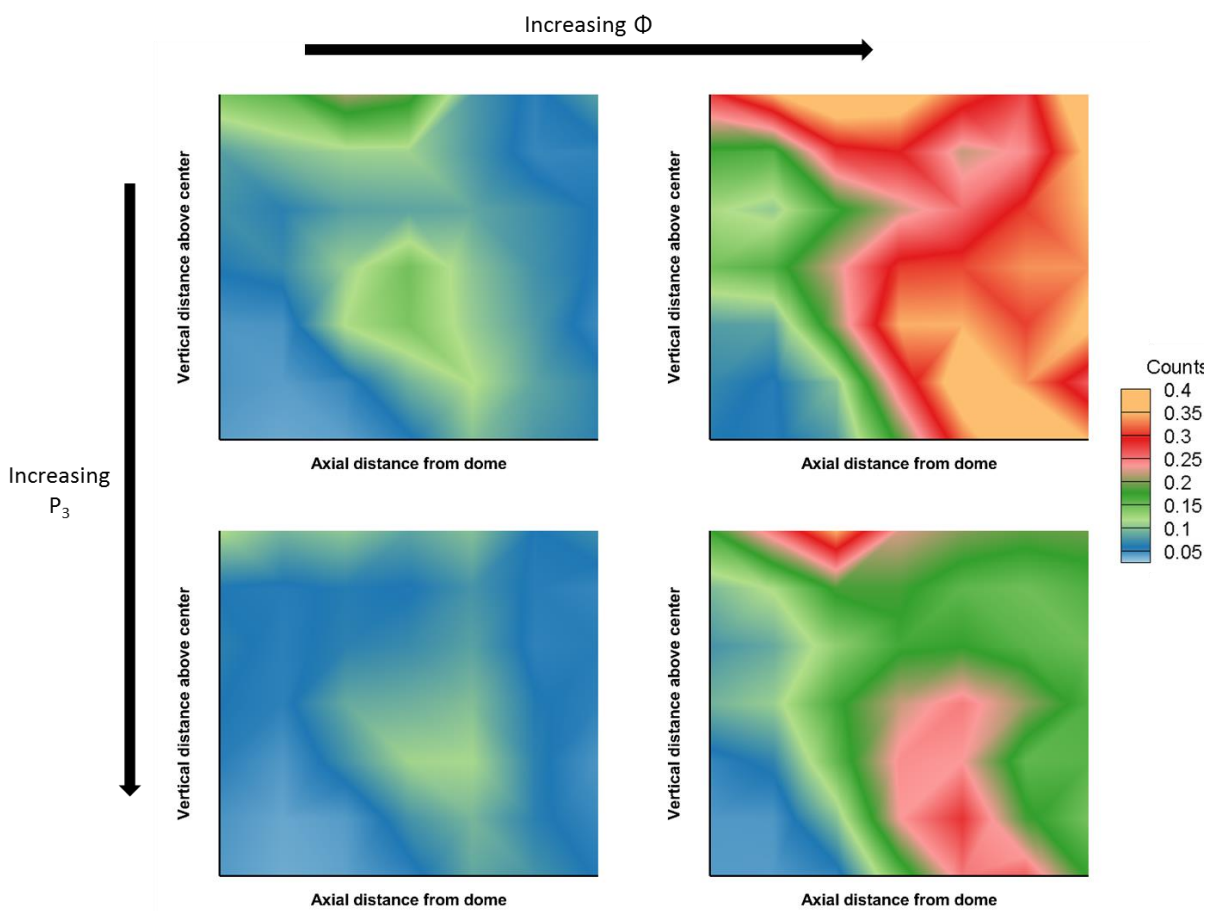

Figure *15***. Species map for NO created by taking ratio of the area under NO by area of N_2. Perspective is aft looking forward into the combustor.**

\

The bottom left image of **Error! Reference source not found.**15 is the NO concentration map corresponding to the PLIF image in Figure 14. Although the dimensional scales do not match, the probe areas are the same between Figure 14 and Figure 15. One can observe some resemblance between the OH PLIF in fgure 14 and the NO species map. Weak OH PLIF was measured in the upstream and downstream sections of the probe area, and slightly stronger OH PLIF within the top and bottom portions of the probe area. This trend is also observed in the corresponding NO map shown in the bottom left image of Figure 16.

Four of the 10/90 split conditions are shown in Figure 15. Left to right, the conditions become richer, and top to bottom P_3 was increased. The top row has P_3 of 150 psia, and the bottom row has P_3 of 250 psia. From both rows, the effect of equivalence ratio is apparent. Increasing the equivalence ratio increased NO considerably. This effect makes sense as higher equivalence ratios lead to hotter flames; therefore, there was more thermal NO.

The effect of P_3, which is demonstrated by each column in Figure 15, was counterintuitive since higher pressures typically result in higher NOx. In the first column, the higher pressure condition also had a slightly higher measured T_4. The likely explanation is due to collisional quenching of the chemiluminescence. Another explanation for the lower pressure result could stem from fuel atomization. The lower pressure condition had a lower pressure drop across the fuel nozzles, and therefore larger fuel drops. According to [Lefebvre], larger fuel drops generate more NOx due to near-stoichiometric burning at locations near the larger drops.

The second column of Figure 15 also has increasing P_3 from top to bottom. However, the equivalence ratio for the conditions in the top row was higher than in the bottom row. Additionally, the measured T_4 for the top row was higher compared to the bottom. NOx is typically more temperature dependent, so this comparison makes sense.

Conclusion

An investigation on the performance of research hardware of a GE TAPS injector was completed in this paper. In order to accomplish this, several optical and laser-based techniques were used to visualize the injector's output behavior. The principal effort aimed to examine fuel spray patternation and flame structure of the reaction zone under several different inlet conditions.

PLIF of fuel and OH are indicative of fuel spray patternation. Fuel PLIF images showed near symmetric distribution about the center position located within the annulus of the injector. In particular, the split conditions of 20/80 and 10/90 had very similar fuel patternation and appeared more evenly distributed compared to the 60/40 condition. In terms of the OH PLIF, the 60/40 split condition indicated a bimodal axial distribution and showed most of the signal from the outside fuel PLIF location. OH PLIF in the 20/80 split showed better distribution compared to the 10/90 split. The 10/90 splits, in particular, showed little OH within the inner cone.

From the chemiluminescence images, we saw that NO^* tracked reasonably well within OH^* between all fuel split conditions. A substantial difference in the flame structure was observed from the 100/0 and 60/40 splits versus the 20/80 and 10/90 splits. The high pilot flow conditions revealed the flame reactions extending the full axial extent of the field of view, which is consistent with fuel-rich flames. In addition, the higher pilot flow conditions showed moderately high concentrations of C_2^* and CH^* near the dump plane; these species also peak at the trailing edge of the

field of view. Between these areas of peak concentrations, OH^* formation was highest. It is noteworthy that the NO^* also peaked within this OH^* region.

PDI measurements probed a location near the TAPS centerline. The PDI setup did not allow access to the dump plane, which is where strong reverse flow might be expected. From the PDI results, there was a central zone of lower velocity which increased outward from the center, which is consistent with conical fuel sprays. Drop sizes distributions at locations upstream and further downstream showed most drops had a mean diameter of about 50 um. Axial velocities of several drop sizes also showed that relatively few droplets travel upstream, indicative of a region probed downstream of the CRZ. Axial-vertical and axial-horizontal slices from the PIV results indicated that a recirculation zone was present. In particular, we observed a recirculation region near the dome within a shear layer between the pilot and mains.

Normalized NO species maps were created from the Raman spectra for four of the 10/90 split conditions. These were done by taking the ratio of the area under the NO peak by the area under the Stokes N_2 line. From these results, the effect of increasing equivalence ratio caused an increase in NOx. The trend in P_3 for splits with the same equivalence ratios showed increasing P_3 resulted in decreased NO. One might expect higher NO with higher pressure. However, one explanation for higher NO under the lower pressure condition could involve poorer fuel atomization. Larger drops can generate more NOx due to near-stoichiometric burning that occur close to the drops.

Acknowledgments

This work was supported by the Advanced Air Transport Technology Project of the NASA Aernautics Research Mission Directorate. We acknowledge our industry partners at GE Aviation.

References

[1]Lee, D.S., Pitari, G., Grewe, V., Grierens, K., Penner, J.E., Petzold, A., Prather, M.J., Schumann, U., Bais, A., Berntsen, T., Iachetti, D., Lim, L.L., and Sausen, R., *Atmospheric Environment*, Vol. 44, 2010, pp. 4678–4734.

[2]Bulzan, D., "Supersonics Project High Altitude Emissions Overview," 2012 Fundamental Aeronautics Program Technical Conference, 2012.

[3]Lee, C.-M., Chang, C., Kramer, S., and Herbon, J.T., "NASA Project Develops Next Generation Low-Emissions Combustor Technologies," Paper AIAA-2013-0540, 2013.

[4]Mongia, H.C., "TAPS—A 4th Generation Propulsion Combustor Technology for Low Emissions," Paper AIAA 2003-2657, 2003.

[5]Foust, M.J., Thomsen, D., Stickles, R. Cooper, C. and Dodds, W., "Development of the GE Aviation Low Emissions TAPS Combustor for Next Generation Aircraft Engines," Paper AIAA 2012-0936, 2012.

[6]Stickles, R. and Barrett, J., "TAPS II Combustor Final Report—Technology Assessment Open Report," FAA Continuous Lower Energy, Emissions and Noise (CLEEN) Program, Report number DOT/FAA/AEE/2014-03, 2014.

[9]Colket, M. et al., "An Overview of the National Jet Fuels Combustion Program," Paper AIAA 2016-0177, 2016.

[15]Winchester, N., McConnachie, D., Wollersheim, C., and Waitz, I.A., "Economic and Emissions Impacts of Renewable Fuel Goals for Aviation in the US," *Transportation Research Part A*, Vol. 58, 2013, pp. 116-128.

[16]Wey, C., and Bulzan, D., "Effects of Bio-Derived Fuels on Emissions and Performance Using a 9-Point Lean Direct Injection Low Emissions Concept," GT2013-94888, 2013.

[17]Hicks, Y.R. and Tacina, K.T., "Comparing a Fischer-Tropsch Alternate Fuel to JP-8 and Their 50-50 Blend: Flow and Flame Visualization Results," NASA TM-2013-217884, 2013.

[20]Baranger, P., Orain, M., and Grisch, F., "Fluorescence Spectroscopy of Kerosene Vapour: Application to Gas Turbines," Paper AIAA 2005-828, 2005.

[21]Hicks, Y.R., Locke, R.J., Anderson, R.C., Zaller, M., and Schock, H.J., "Imaging Fluorescent Combustion Species in Gas Turbine Flame Tubes: On Complexities in Real Systems," Paper AIAA 97-2837, 1997.

[22]Friedel, R.A., and Orchin, M., *Ultraviolet Spectra of Aromatic Compounds*, Wiley & Sons, New York, 1951, pp. 12-14.

[23]Berlman, I.B., *Handbook of Fluorescence Spectra of Aromatic Molecules*, 2nd ed., Academic Press, New York, 1971, Chaps. 3-4, pp.114-115, 330.

Nori, V. and Seitzman, J., "Evaluation of Chemiluminescence as a Combustion Diagnostic under Varying Operating Conditions," Paper AIAA 2008-953, 2008.

Guiberti, T.F., Durox, D., and Schuller, T., "Flame Chemiluminescence from CO2- and N2-diluted laminar CH4/air premixed flames," *Combustion and Flame*, Vol. 181, 2017, pp. 110-122.

Guyot, D. et al, CH*/OH* Chemiluminescence Response of an Atmospheric Premixed Flame under Varying Operating Conditions, GT2010-23135, 2010.

Kojima, J, Ikeda, Y., and Nakajima, T., "Basic aspects of OH(A), CH(A), an dC2(d) chemiluminescence in the reaction zone of laminar methane-air premixed flames," *Combustion and Flame*, Vol. 140, 2005, pp. 34-45.

Reisel, J. and Laurendeau, N….

Thomsen, D. and Laurendeau, N…

Cooper, C., and Laurendeau, N…